Chapter 31

Application of Inverse Scattering and Other Refraction Corrected Methods to Environmental Imaging with Acoustic or Electromagnetic Energy[1]

STEVEN A. JOHNSON,[2] DAVID T. BORUP,[3] JAMES W. WISKIN,[3] MICHAEL J. BERGGREN,[3] MICHAEL S. ZHDANOV,[4] KYLE BUNCH,[5] AND RICHARD EIDENS[3]

Abstract

There are several advantages of inverse imaging over present standard imaging methods such as improved spatial resolution, freedom from multiple scattering and reverberation artifacts, and true quantitative imaging. We verify these advantages and illuminate the progression from theory to simulation, to laboratory experiments, and finally to planned field experiments. We show examples of inverse scattering in radar, sonar, and low-frequency electromagnetic (EM) radiation in a geophysical context, and compare these images with conventional methods. We discuss the importance of calibration in order to implement inverse scattering procedures, and explain how such calibration is effected. We summarize the requirements for proper implementation of inverse scattering imaging and point out where such methods will yield real benefits over standard imaging techniques. The paper also enumerates the factors required for the development of practical field inverse scattering imaging devices.

31.1 Introduction

Computer modeling of environmental problems and their solutions is often applied to two important classes of problems:

- *Modeling of flow and diffusion of natural and manmade materials.* Examples of such flow and diffusion problems are

  - solution of the weather prediction problem, but in particular prediction of wind patterns;

  - prediction of ocean currents and their coupling with weather patterns;

  - prediction of flow of ground water; and

  - prediction of flow of toxic spill materials [4].

- *Modeling of diagnostic probing radiation and extraction of environmental site information.* Modeling of diagnostic probing radiation is an example of solving the so-called *forward scattering problem.* Here, the word scattering is used in a general sense and includes prediction of transient fields, time harmonic fields, and static fields. Such fields can be electromagnetic acoustic, elastic, and even composite fields such as are used in magnetic resonance imaging. The modeling of probing radiation is valuable for predicting the response of the environment to probing radiation. The forward scattering problem is a part of the more difficult *inverse scattering problem,* wherein the spatial distribution of the material properties that cause scattering are sought by computational means; thus a quantitative image of the scattering model is sought. In the remainder of this paper we focus on this second class of problems. Our approach has been described in a series of papers [2, 3, 7, 8, 18, 19, 20].

In the direct scattering problem, a selected computer simulation model of the environment is probed by radiation and the response is evaluated for closeness of match to that observed from real field data. If the match is close, then one can say at least that the model is a likely candidate for the true environment. If, in addition, the model fits multiple sets of independent data collected from field data at the same environmental site (e.g., different source and receiver positions at different temporal frequencies) then the likelihood of an accurate match of the model to the truth is improved. Confidence in the accuracy of the selected model(s) becomes very high if models similar in some respects, yet different in others, produce forward scattered data that do not match the field data. This trial and error approach is often used as a simple and intuitive method to find a close match to the true distribution of scattering parameters. This approach is reasonable for simple geometries or when a priori information about the environment is known. For more complex environments, a more analytical and systematic approach, such as inverse scattering, is useful.

The solution to the inverse scattering problem supplies a direct, deterministic, calculated estimation of the spatial distribution of the material properties (the scattering potential) that cause scattering. In ideal situations, with sufficient data and with appropriate active constraints, this solution provides an accurate, fully resolved, quantitative image of the scattering potential. In other words, the solution is unique. However, in many cases, these ideal conditions are not met (for example, data are sparse or the problem is not sufficiently constrained). In these cases, the images formed will show distortion, lack of accuracy, or mixing of scattering potential components.

Table 31.1

Green's Operator and Scattering Potential for Acoustic and Electromagnetic Cases.

Name	Symbol	Acoustic case	Electromagnetic case
Field	$\mathbf{f}_{\omega\phi}(\mathbf{x})$	$\mathbf{f}_{\omega\phi}(\mathbf{x})$	$\mathbf{E}_{\omega\phi}(\mathbf{x})$
Green's Operator	$G_{\omega}(\mathbf{x}-\mathbf{x}')$	$G(k_o,\mid \mathbf{x}-\mathbf{x}'\mid)$	$(k_o^2+\nabla^2)G(k_o,\mid \mathbf{x}-\mathbf{x}'\mid)$
Scattering Potential	$\Gamma_{\omega}(\mathbf{x})$	$\left[1-\frac{c_o^2}{c^2(\mathbf{x})}\right]+$ $\frac{\omega^2}{c_o^2}\cdot\rho^{\frac{1}{2}}(\mathbf{x})\nabla^2\rho^{-\frac{1}{2}}(\mathbf{x})-\frac{i2c_o^2\alpha(\mathbf{x})}{\omega c(\mathbf{x})}$	$\left[\frac{\varepsilon(\mathbf{x})}{\varepsilon_o}-1\right]-i\left[\frac{\sigma(\mathbf{x})}{\omega\varepsilon_o}\right]$

We now present a symbolic derivation of the relationship between the solutions of the forward and inverse scattering problems and discuss applications. We shall use the volume integral equation formulation of the wave equation as an example of this relationship. We note that some high contrast problems involving discrete objects require the use of extra surface integral terms to supplement the volume integral terms.

The most general form of the Lippmann–Schwinger volume integral scattering equation

$$\mathbf{f}_{\omega\phi}^{inc}(\mathbf{x})=\mathbf{f}_{\omega\phi}(\mathbf{x})-\int_S G_{\omega}(\mathbf{x}-\mathbf{x}')\cdot\left\{\Gamma_{\omega}(\mathbf{x}')\mathbf{f}_{\omega\phi}(\mathbf{x}')\right\},\;\mathbf{x}',\mathbf{x}\in\Re^n \tag{1}$$

is presented, along with examples of applications. By choosing different Green's functions G_{ω} (or dyadics) and scalar (or vector) fields $\mathbf{f}$, one can simulate scattering for acoustic, elastic, and electromagnetic fields in one to four dimensions. The scattering object with bounded support, S, is defined by the scattering potential, or operator Γ_{ω}, which is composed of the relevant material parameters. The subscript ω denotes the angular frequency. The vector $\mathbf{f}$ consists of the components of the induced total field and $\mathbf{f}^{inc}$ is the incident field. The subscript ϕ denotes a particular source position (view). The Green's operator, G_{ω}, is shift invariant if scattering occurs in a homogeneous space, but is more complicated in general. Exploitation of this shift invariance plays a crucial role in the numerical efficiency of our algorithm. Equation (1) can be solved uniquely for the total field, $\mathbf{f}$, given $\mathbf{f}^{inc}$ and Γ_{ω}. These equations are referred to as the *total field equations* and Table 31.1 shows the specific form of the fields, Green's operator, and scattering potential for the acoustic (scalar field and operator) and electromagnetic (vector field and dyadic operator) cases, respectively.

Let a set of measurements of the scattered field, $\mathbf{f}^{scat}=\mathbf{f}-\mathbf{f}^{inc}$, be made at a set of N_d detector locations for Φ views and Ω frequencies. Then the *detector equations* are given by

$$
\begin{aligned}
\mathbf{f}_{\omega\phi}^{scat}(\mathbf{x}_d) &= \int_S G_{\omega}(\mathbf{x}_d-\mathbf{x}')\cdot\left\{\Gamma_{\omega}(\mathbf{x}')\mathbf{f}_{\omega\phi}(\mathbf{x}')\right\}, \\
d &= 1,...,N_d,\;\phi=1,...,\Phi,\;\omega=1,...,\Omega.
\end{aligned}
\tag{2}
$$

The general nature of these relationships is illustrated in Table 31.1 for acoustic and electromagnetic cases. In Table 31.1: c_o and $c(\mathbf{x})$ are phase speeds in the background and perturbed material, respectively; $\rho(\mathbf{x})$ is density; $\alpha(\mathbf{x})$ is acoustic absorption; ε_o and $\varepsilon(\mathbf{x})$ are the permittivity in the background and perturbed material, respectively; and $\sigma(\mathbf{x})$ is the conductivity. If (1) is written symbolically as $(\mathbf{I}-G_{\omega}\{\Gamma_{\omega}\})\mathbf{f}=\mathbf{f}^{inc}$, then the field $\mathbf{f}$ which is the solution to the forward scattering problem, is given by

$$\mathbf{f} = (\mathbf{I} - G_\omega\{\Gamma_\omega\})^{-1}\mathbf{f}^{inc}. \qquad (3)$$

Equation (2) is written symbolically as

$$(G_\omega\{\Gamma_\omega\})\mathbf{f} = \mathbf{f}^{scat}. \qquad (4)$$

If (3) is substituted into (4), the result is $(G_\omega\{\Gamma_\omega\})\ (\mathbf{I}- G_\omega\{\Gamma_\omega\})^{-1}\mathbf{f}^{inc} = \mathbf{f}^{scat}$. The solution to the inverse scattering problem is found by solving this last equation for Γ_ω. This is conveniently done by optimization methods using conjugate gradients or related techniques. The solution is the Γ which minimizes the square of the L_2 norm of the difference between the predicted and measured scattered fields [2, 7, 8, 18, 19, 20]

$$\Gamma = \min_\Gamma \| (G_\omega\{\Gamma_\omega\})(\mathbf{I} - G_\omega\{\Gamma_\omega\})^{-1}\mathbf{f}^{inc} - \mathbf{f}^{scat} \|^2 . \qquad (5)$$

The solution from equation (5) is at a single frequency only. Time domain solutions are found by inverse Fourier transforming a set of such harmonic solutions (direct time domain solution methods have been described in [17]). In the case of using the inverse Fourier transform, it is sometimes important to incorporate physical constraints such as the Kramers–Kronig relations to increase the quantitative accuracy of the reconstructed images [13]. We now demonstrate a series of applications and examples that use this approach; they are taken from computer simulations of ground penetrating radar, seismic and sonar imaging, low-frequency electromagnetic (EM) imaging, and from data collected in the laboratory.

31.2 Advanced ground penetrating radar

31.2.1 Introduction to features of advanced ground penetrating radar

The projected advantages of applying inverse scattering methods to ground penetrating radar (GPR) are significant:

- a maximum spatial resolution of half a wave length at the highest frequency component,

- quantitative imaging of material phase speed and absorption, and

- removal of reverberation and speckle artifacts.

The price that must be paid to obtain these advantages includes the following requirements:

- calibration of the transmit antenna beam pattern in the near field,

- calibration of the receiver antenna sensitivity pattern in the near field,

- calibration of other components of the system transfer function,

- development of dielectrically loaded, wide bandwidth antennas that couple directly to the earth (this eliminates the problem of critical angle reflections using air loaded antennas), and

- development of integrated high-speed digitizers and computational hardware.

Since the above requirements are formidable, we adopted a two-pronged approach that includes

- development of improved methods intermediate between the present GPR and full inverse methods, and
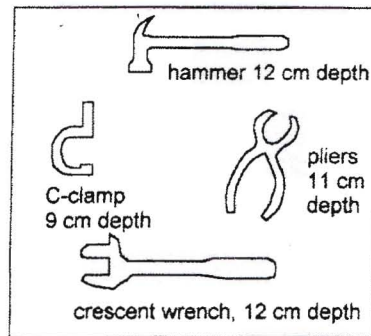
FIG. 31.1. *Illustration of the arrangement and depth of burial in sand of various metal objects.*

- development of full inverse scattering methods.

The first prong of this approach is based on augmenting and improving common GPR. GPR is often used only to display raw reflectivity data (echo strength versus time versus lateral displacement of radar antenna). The value of this data is enhanced if it is used to form images by various linear processes such as migration, beam forming, or backprojection. Image quality can be further improved by addition of further advanced features such as

- correction for refraction and absorption,

- collection of data on two-dimensional (2-D) grids to form three-dimensional (3-D) images, and

- use of advanced visualization methods to display 2-D and 3-D images.

Correction for refraction in the first prong approach is a very important feature and can be done one of two ways [1, 6, 9, 10, 11, 12, 14, 15, 16]:

- introduced as an ad hoc model, or

- estimated from the data (use of phase aberration correction).

The first approach, using a given model, is applied to making the image in Figure 31.1.

The second prong of our approach for demonstration of advanced GPR through inverse scattering requires a more studied and incremental approach. Unlike ordinary GPR, theory for inverse scattering GPR requires that the calibration of the antennas and the total system be included in the inversion process. If calibration is done properly, then accurate assumption about the background media are not required or are minimal relative to ordinary GPR. Calibration issues were approached in three steps:

- imaging studies including both simulated single frequency data and simulated multiple frequency reflection data using point sources and receivers where calibration is not an issue,

- imaging from a laboratory scanner using a single frequency and 360 degree scattering data (nonpoint source, requiring calibration), and

- imaging from laboratory scanning using multiple frequencies and reflection mode data (nonpoint source, requiring calibration).

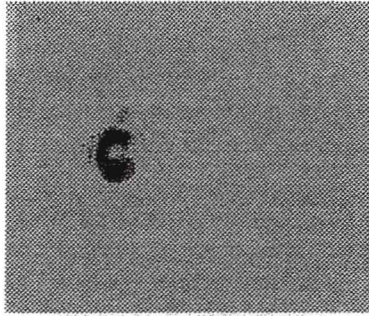These three steps are described in Section 31.2.3 below.

FIG. 31.2. *Excellent microwave image of C-clamp at 9 cm depth in sand. The data set was collected on a 61×61 point scan grid using 401 frequencies between 1 GHz and 18 GHz and bistatic antennas with fixed separation of 27 cm for a step size of 1 cm in x and y.*

FIG. 31.3. *A microwave image made at 15 cm depth in sand. Note that the C-clamp shows almost zero reflected power at this depth, while the deeper objects are detected (pliers, crescent wrench, hammer).*

31.2.2 Simple reflection mode imaging from real data

Figures 31.1-31.3 show progress in forming 3-D, GPR images made by correcting for Snell's law of refraction at the surface of the soil/air interface. The computed 3-D image is displayed by use of a commercial visualization program called *Spyglass* [5] that is an extension of an earlier program called *Image* developed at the National Center for Supercomputer Applications (NCSA) at the University of Illinois. The data set was collected using two broad-band antennas, in bistatic mode, operating from 1 to 18 GHz, and coupled to an HP 8720C network analyzer. The antennas scanned as a pair, with fixed separation, in a 2-D pattern of 60 cm by 60 cm with 1 cm increments. A frequency sample separation of 42.5 MHz gave a range of 23.5 nanoseconds that corresponds to $r = \frac{1}{2}ct = \frac{1}{2}(300m/\mu s)(0.0235\mu s) = 3.5m$. The targets are metal tools (C-clamp, hammer, crescent wrench, pliers) buried from 9 cm (C-clamp) to 13 cm (wrench) below the surface of the sand. The measured dielectric constant $K = \frac{\varepsilon}{\varepsilon_o} = n^2 = (\frac{c_o}{c})^2$ is 2.35. The index of refraction $n = \sqrt{2.35} = 1.53$ and the depth spatial resolution is $\frac{c}{2nB} = \frac{0.3m(ns)^{-1}}{2n\cdot17(ns)^{-1}} = 8.8mm$. Here, B is bandwidth, c_o is phase speed in air, and c is phase speed in sand. The lateral spatial resolution is limited by the numerical aperture given by Snell's law for refraction at the sand/air interface. The wave length in sand is $\lambda = \frac{\lambda_o}{n} = \frac{c}{f}$. For a rectangular
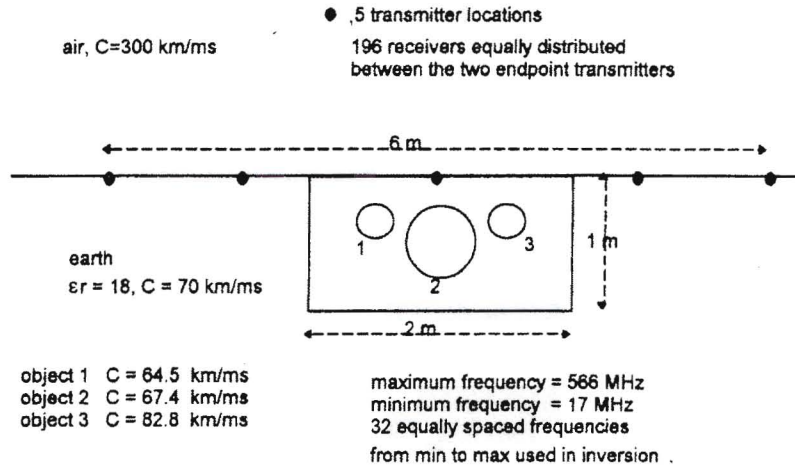
● .5 transmitter locations

196 receivers equally distributed
between the two endpoint transmitters

air, C=300 km/ms

earth
εr = 18, C = 70 km/ms

6 m

1 m

2 m

object 1   C = 64.5 km/ms
object 2   C = 67.4 km/ms
object 3   C = 82.8 km/ms

maximum frequency = 566 MHz
minimum frequency = 17 MHz
32 equally spaced frequencies
from min to max used in inversion .

FIG. 31.4. *A simulation model was constructed (as shown) of three cylindrical objects with differing radar velocities, imbedded in an earth halfspace. The phase speed of radar (which brackets that of earth) is shown for air, earth and the three cylinders.*

aperture, the spatial resolution (for the first zero crossing with one antenna) is given by $\Delta x = \lambda / \sin(\frac{1}{2}\phi_{sand})$, where $\frac{1}{2}\phi_{sand}$ is the full aperture angle. Let the angular beam width of the antenna in air be θ_{air} and let $\frac{1}{2}\phi_{sand} = \theta_{sand}$. Then Snell's law gives $\sin\theta_{air} = n\sin\theta_{sand}$, and $\Delta x = \frac{\lambda_o}{n}\frac{n}{\sin\theta_{air}} = \frac{\lambda_o}{\sin\theta_{air}}$. For $n = 3$, $\theta_{air} = 45^o$, and $f = 18$ GHz, the lateral spatial resolution $\Delta x = 23.6mm$.

Using dielectrically loaded antennas to provide direct coupling into the ground would give n times better spatial resolution, i.e. (for $n = 3$), $\Delta x = 23.6/3 = 7.86mm$. Further improvement in signal-to-noise ratio and speckle reduction can be achieved by collecting a data set with multiple offset distances between the transmitter and receiver.

31.2.3   Imaging from simulated data

We now present a simulation example that indicates the promise of inverse scattering approaches over conventional GPR methods. Inverse scattering would provide quantitatively accurate images of material properties, corrected for diffraction, refraction, and reverberation effects, and would provide much greater information for material characterization and the undistorted imaging of object shape.

Scattering data for a set of transverse mode (TM) polarized line transmitters and receivers was generated by solving our integral equation (IE) formulation of the forward scattering problem over a bandwidth of 17 to 566 MHz at 32 equally spaced frequencies. The model used is shown in Figures 31.4 and 31.5. The image made (using very wide band radar) is shown in Figure 31.6 and is excellent in the categories of spatial resolution, freedom from artifacts, and quantitative accuracy. The image shown in Figure 31.7 (using medium bandwidth) is less accurate and has some artifacts, but has good spatial resolution and is, nevertheless, still quite good.

The image shown in Figure 31.8 was made using standard radar backprojection (using an adapted seismic migration program incorporating refraction correction) and is of poor quality in comparison with that of Figure 31.7. The spatial resolution is fair to good in
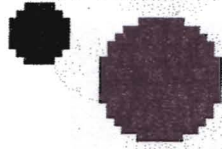
FIG. 31.5. *Gray scale image of the true $\gamma(\mathbf{x}) = \varepsilon_r(\mathbf{x}) - 1$, where ε_r is the dielectric constant relative to the earth imbedding. A 64×32 pixel model was used with a pixel dimension of $\frac{1}{4}\lambda$ at 566 MHz for a grayscale range of $\gamma = 0.2$ (black) to $\gamma = -0.1$ (white).*
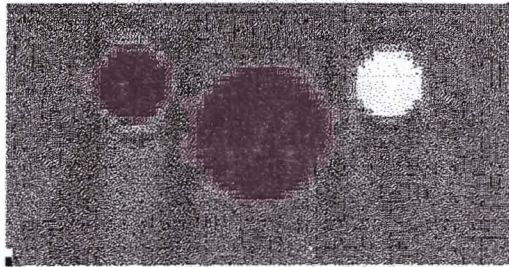

FIG. 31.6. *Gray scale image of the inverse scattering reconstruction of $\gamma(\mathbf{x}) = \varepsilon_r(\mathbf{x}) - 1$, where ε_r is relative to the earth imbedding for a gray scale range of $\gamma = 0.2$ (black) to $\gamma = -0.1$ (white). Full bandwidth from 17 to 566 MHz was used (32 frequencies) and the reconstruction is nearly perfect. The depth is $\frac{1}{4}\lambda_{min}$ at 17 MHz.*
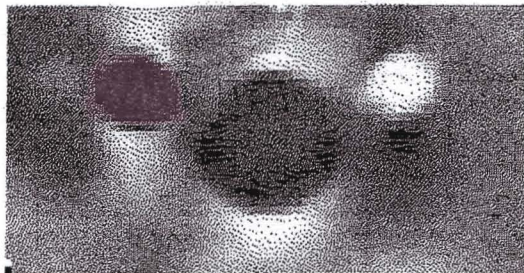
FIG. 31.7. *Gray scale image of the reconstructed $\gamma(\mathbf{x}) = \varepsilon_r(\mathbf{x}) - 1$, where ε_r is relative to the earth imbedding for a gray scale range of $\gamma = 0.2$ (black) to $\gamma = -0.1$ (white). Partial bandwidth from 70 MHz to 566 MHz was used (29 frequencies) and in this case note the slight blurring and loss of quantitative accuracy relative to Fig. 31.6. This is caused by the decrease in bandwidth (loss of low-frequency information). The depth is λ_{min} for 70 MHz.*
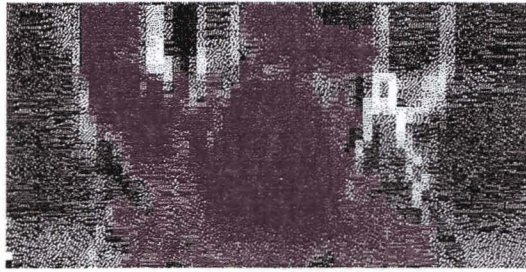
FIG. 31.8. *Grayscale image of the backprojection of the simulated data. This approach produces an image of "reflectivity" — a nonquantitative parameter that reveals interface reflections only. Present state-of-the-art GPR units produce images of this type.*

some regions but poor in other regions. Both target number 1 and 2 are easily seen but target number 3 is invisible. The bottom of target number 1 is visible but its top is not. These results indicate the greater power of inverse scattering to make improved images over standard GPR.

31.2.4 Laboratory inverse radar imaging of a buried ABS pipe in reflection mode with ridged horns

The x, y scanning apparatus used to make the noninverse images, shown in Figures 31.1 to 31.3, was also employed in Figures 31.4 to 31.8. The challenge is that laboratory antennas cannot be modeled as point sources and receivers. This problem can be solved by calibrating each antenna to produce a representation of the incident field pattern produced by the transmitting antenna and a sensitivity pattern for the receiving antenna. These patterns must be accurate in spatial extent. The antennas were moved to 60 cm above the sand to avoid antenna-sand reverberations and to simplify the field pattern in the vicinity of the target. Since our scanner is too low for this range, the antennas were mounted on a wooden scaffold in a fixed position above the sand. The geometry is shown schematically in Figure 31.9.

The spectral calibration procedure was as follows. First, the sand was covered with microwave absorber so that the only signal present was the direct wave between the transmitter and receiver horns. This signal was recorded for later subtraction. Then, the sand was covered with an aluminum sheet. The network analyzer was then calibrated to subtract the direct wave and then divide by the aluminum reflection spectrum. This has the effect of giving a perfect delta function for the aluminum reflection at $t = 0$. Since the sand reflection is similar in spectrum to the aluminum, this procedure ensures that the signal from the sand is compressed in time at $t = 0$ (it is "almost" a delta function). This procedure is designed to try to maximize our ability to see the target reflection without being obscured by the sand-air interface signal. The target is a 3.5 inch air-filled ABS pipe and the resulting data as a function of time is shown in the top trace of Figure 31.10. Note that the calibration procedure has resulted in the desired very good separation between the sand surface reflection and the tube signal.

Also shown in Figure 31.10 is a 2-D simulated time trace using the following assumptions:

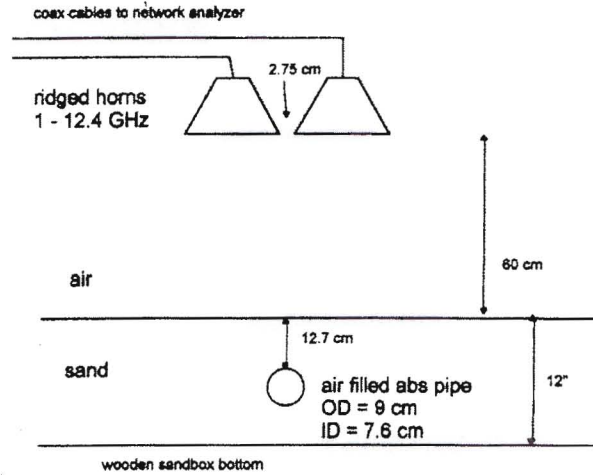- the simulation is 2-D, consisting of a line source transmitter and a line source receiver

FIG. 31.9. *Geometry of the experiment showing two-wide band (1 to 12.4 GHz) ridged horns mounted side by side in a fixed position 60 cm above a 5 ft.×4 ft. box filled with 12 in. of sand. An air-filled PVC pipe with 9 cm outer diameter (OD) and 7.8 cm inner diameter (ID) is buried 5 inches deep (to its top surface). The antennas are connected to a network analyzer scanning from 1 to 12.4 GHz in 0.057 GHz steps (201 frequencies). The dielectric constant of the sand was determined by transmission experiments to be 2.35 with negligible conductivity (very dry sand). The γ of the plastic relative to the sand is $\varepsilon_r^{ABSplastic}/\varepsilon_r^{sand}-1=2.6/2.35-1=0.106$. The dielectric constant of the air relative to the sand is $\varepsilon_r^{air}/\varepsilon_r^{sand}-1=1/2.35-1=-0.57$. We define the parameter to be imaged as $\gamma = \varepsilon_r^{target}/\varepsilon_r^{sand}-1$, which is zero outside the target.*
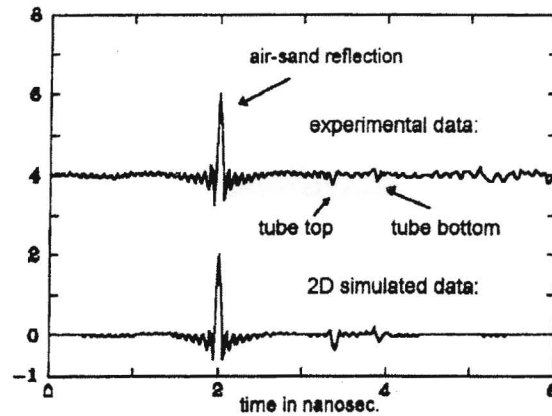

FIG. 31.10. *Comparison of the lab data with 2-D theory for the experiment in Figure 31.9. The top trace is the frequency domain experimental data transformed to time. The large sand reflection and smaller top and bottom pipe reflections are evident. The lower curve shows a time trace generated by a 2-D simulation of the geometry. At this point, a fair amount of clutter, most likely from other scatterers, is evident in the lab data. The weaker signal strength of the data versus the simulation is due to improper scaling between the simulation theory and the experiment.*
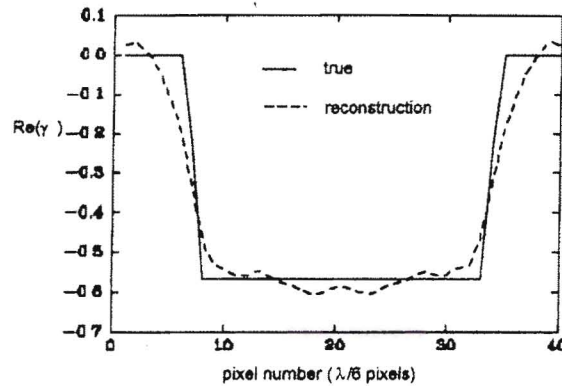
FIG. 31.11. *Centerline profile comparison of the true and reconstructed γ's.*

located at the same x, y positions as the feed elements in the horns, and

- the spectrum of the simulation is calibrated to give the same sand interface signal as that observed in the data.

The main discrepancy between the data and simulation is that the ratio of the tube/sand signals is smaller in the data than in the simulation. The overall waveform shape comparison is quite good, however. At this point, this amplitude discrepancy was thought to originate from the use of the aluminum reflection to calibrate the theory and experiment. Since the sand reflection signal derives from a large angular segment of the antenna radiation pattern, it may not satisfy the 2-D cylindrical wave approximation very well.

The data was processed with an inverse scattering algorithm employing a constraint that forced the object to have cylindrical symmetry. Figure 31.11 shows a line plot comparison of the true and reconstructed objects on the center axis.

31.3 Advanced seismic and sonar imaging

To compare standard sonar and inverse imaging methods using simulated data, we also performed reconstruction (using inverse scattering) for a rough surface in addition to the random perturbations in the sediment itself. For this simulation, however, we used the layered Green's function, which accounts for the head wave phenomena and other interfacial wave effects. The random perturbations were instituted in the same manner as previously (with the sinc-convolved Gaussian random distribution). The background speed of sound c_o is in this case the sediment speed of sound, namely, 1711 m/sec. Therefore the γ values for the spherical shell and for the interior of the mine must be different from the previous case. In particular, the γ inside of the mine is -0.1449. The γ for the spherical shell is -0.499, and that for sea water is 0.251.

The aperture in this scenario was severely limited, compared to the case above. The scenario and its geometry are as shown in Figure 31.12. A cylinder is buried below a rough surface. The rough surface is added to simulate a worst case. Also included is a random speed of sound in the space to be imaged. In order to see the effect of the random background, two sets of simulated data were made, both with a random surface. The first set has no random background, while the second set does. An example of the first set of data is shown in Figure 31.13, while the corresponding image made by backprojecting
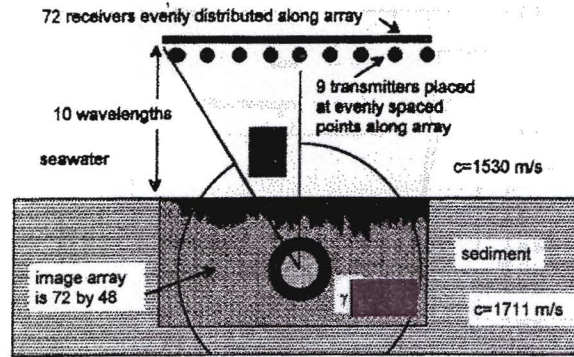
FIG. 31.12. *Geometry for simulation of inverse scattering imaging of a buried object in random media with a rough surface. The image area is 72×48 pixels and each pixel is $\frac{1}{6}\lambda$ for λ corresponding to sea water and here $\theta = \arctan(\frac{6}{14}) = 23.2$ degrees. The average speed in image array is 1711 m/s with a standard deviation of 17 m/s. The shell wall speed is 2400 m/s and shell center speed is 1850 m/s.*

FIG. 31.13. *Data from the first transmitter and all 72 receivers in an array located 10 wavelengths above the bottom (at 150 kHz). No random background in the object was used, but a random surface was included. The phase speed of sediment was set equal to that of sea water.*

(beam forming) with normal radar migration is shown in Figure 31.14. The image is not good, but still, the average location of the rough surface is visible and the top and bottom of the cylinder can be identified. The corresponding data and migrated image, with the random background turned on, is shown, respectively, in Figures 31.15 and 31.16. Note how the random background has added complex background artifacts to the data and the image, so the surface of the sediment and the cylinder can no longer be identified.

The dramatic improvement in image quality by the use of inverse scattering is shown in Figure 31.17. The left panel shows the starting image containing the random background
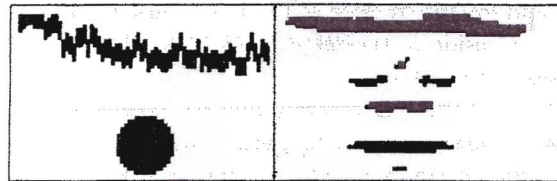

FIG. 31.14. *In the left frame the object is below the random surface in nonrandom media (sea water). The right frame shows the reconstruction by beam forming using data from the previous panel.*

FIG. 31.15. *Data from 72 receivers using only the 4th transmitter. A random background and a rough surface was used.*
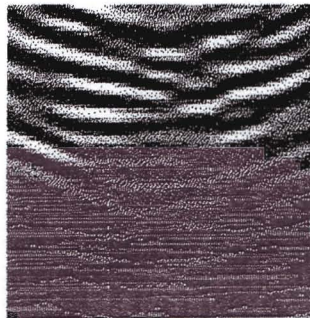

FIG. 31.16. *A back projected (i.e., synthetic focus or migrated) image using data made from an object in a random background and a rough surface.*
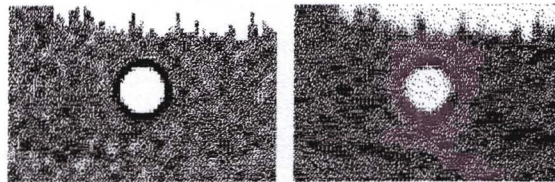

FIG. 31.17. *Model an of object buried in a random sediment below a rough surface is shown on left. The inverse scattering reconstruction is shown on the right. The random rough surface is also reconstructed.*

and random surface. The right panel shows the reconstructed inverse image. Note the excellent-to-good quality of the imaged surface, random background, and the cylinder.

Due to the nature of the layered Green's function used in the reconstruction and in the generation of the data, the basis functions used in the vertical directions could not be the sinc functions. The sinc functions could, however, be used (and were used) in the horizontal direction. Pulse basis functions were used in the vertical direction, resulting in a numerically less well posed problem. The γ_{error} in this case was only 32%, instead of the 10% achieved by the sinc basis function algorithm (for the free space case). Furthermore, the Jacobian employed in the inversion was a Born-like approximation rather than the exact form.

31.4 Advanced low-frequency EM imaging

As a final example of inverse methods, we demonstrate the properties of a potentially very valuable tool for 3-D imaging of the resistivity (reciprocal of conductivity) of the earth at ranges of up to 3 meters. This range cannot be obtained using GPR because of the high absorption at radar frequencies. Using frequencies of 10 kHz to 1 MHz provides the needed penetration, but spatial resolution suffered. Furthermore, at these low frequencies, the size of GPR antennas are large and unwieldy (they are typically half a wavelength in diameter at the lowest frequency component) and are difficult to place in wells or bore holes. However, the special nature of low-frequency electromagnetic energy and circuitry provides at least two compensating factors that allow higher spatial resolution and smaller equivalent antennas than would be predicted by simply scaling down the frequency of common GPR.

The first factor is the capability of small inductive loops or coils (as small as $\frac{1}{10}$ to $\frac{1}{1000}$ the size of a wavelength) to efficiently couple electromagnetic energy into space or the earth. This feature is enhanced when materials with high permeability (such as ferrites) are used as a core on which the coil is wound. The second factor is the use of superresolution that is possible in the near field of the source and receiver antenna (coil). A further factor is the small effective wavelength at these lower frequencies due to the high dielectric constant of soils with high water content and due to the lower speed of propagation of waves in high conductivity media (by Lenz's law, the conductive earth tries to maintain the induced currents rather than letting them propagate unimpeded, as in a vacuum). Spatial resolution of about the size of the coil for neighborhoods within about one wavelength of the antenna coil is possible when using synthetic apertures.

Figure 31.18 shows the geometry of a 2-D distribution of resistivity representing 3 layers of dense nonaqueous phase liquid (DNAPL) contamination. A well, which contains a bistatic antenna, is located 5 meters from the closest edge of the contamination. The offset between transmitting and receiver coils is held fixed at about 1 foot as the antenna pair is lowered down the well to create a synthetic aperture. The current in the transmitting coil is fixed as a step function (with exponential fall-off or as a long period, square wave) to allow the receiver coil to pick up the reflected transient induced field. The rate of decay of features in this transient field provide the encoded range to regions of inhomogeneous resistivity. One would expect that inversion methods would be optimal for imaging the resistivity from these transient data. We have found that the use of migration (back-projection) -type algorithms [21, 22], with an associated change of variable to approximate the reflection coefficient of the soil at each resolvable range bin, provides remarkably good and useful images without full inversion [21]. Figure 31.19 shows the data collected from this geometry. Figure 31.20 shows the migrated image made from these data. Note that the
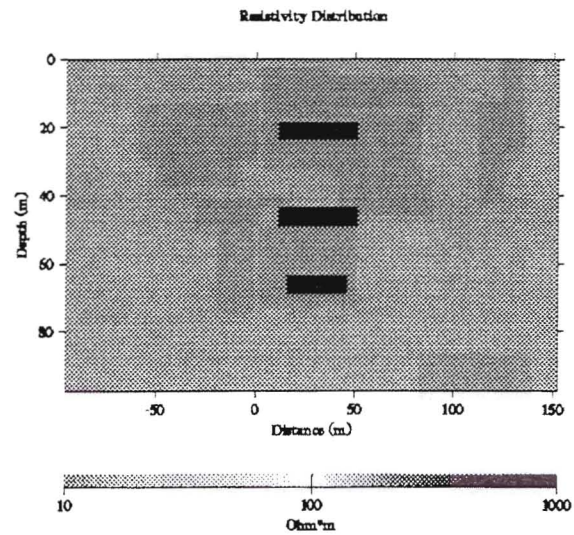
Resistivity Distribution

FIG. 31.18.   *Geometry of a 2-D distribution of resistivity representing three layers of dense nonaqueous phase liquid (DNAPL) contamination.*
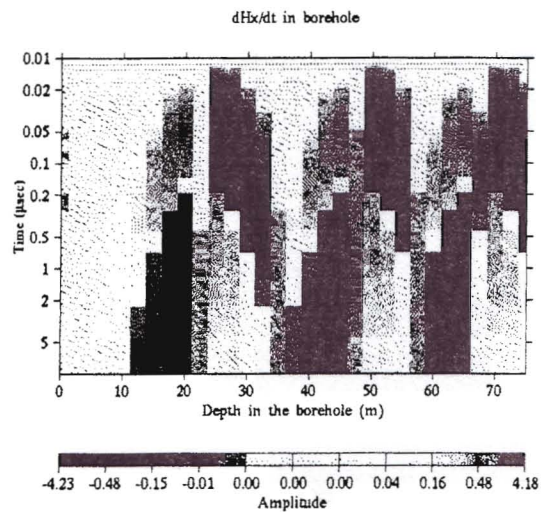
dHx/dt in borehole

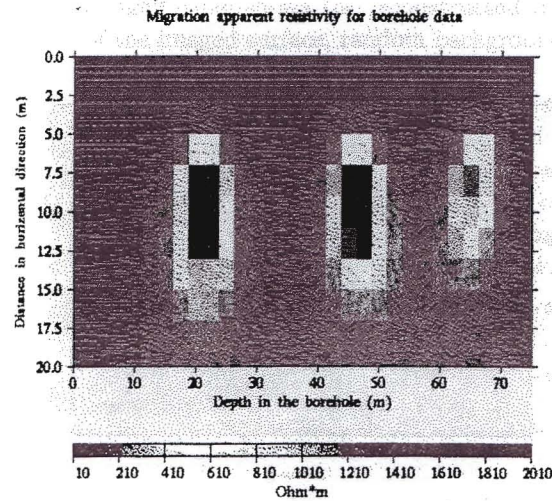FIG. 31.19.   *Geoelectric model of a dense nonaqueous phase liquid showing the data collected from the geometry shown in Fig. 31.18.*

FIG. 31.20. *Geoelectric model of a dense nonaqueous phase liquid showing the migrated image reconstructed from data of Fig. 31.19 for the geometry shown in Fig. 31.18.*

major structures have been resolved and are reasonably quantitatively accurate. Similar reconstructions are obtained with as much as 20 percent noise added to the data.

31.5 Summary and conclusions

In this paper we have described the advantages of inverse imaging over present standard imaging methods. These advantages include improved spatial resolution, freedom from multiple scattering and reverberation artifacts, and true quantitative imaging. We have illuminated the path of progress from theory to simulation to laboratory experiments and planned field experiments. We have shown examples of inverse imaging using radar, sonar, and low-frequency EM probing radiation. For the case of radar and sonar, we have compared the inverse images with conventional images. These comparative images validate the predictions of the advantages of inverse imaging over conventional methods. In order to implement inverse imaging using real data, the characteristics of the source of radiation and the receiver of the scattered radiation (e.g., antennas or transducers) must be combined with the wave equation models. Since these characteristics are not known and are not needed for conventional imaging methods, it is necessary to calibrate the antennas or transducers incorporated into the imaging system. Excellent inverse images have been made using real laboratory data and such calibration procedures and thus illustrate the value of calibration.

The role of inverse imaging in field service depends on several factors:

- replication of the laboratory results at larger field scale,

- implementation using more precise instrumentation to obtain more accurate, and more repeatable data,

- incorporation of antenna or transducer calibration procedures, and

- use of faster computers to reduce the cost of image computation and to allow larger images to calculated.

The development of faster inverse imaging algorithms and even faster approximate inverse imaging algorithms will also be clearly beneficial. The present state of inverse imaging methods and computer speed should allow these powerful methods to be applied in selected examples where the advantages of inverse methods are needed. Further evolution in the speed and efficiency of algorithms and hardware will bring inverse methods to wider application.

ACKNOWLEDGMENTS

References

[1] R.H.T. Bates and P.J. Napier, Identification and removal of phase errors in interferometry, *Monthly Notices of the Royal Astronomical Society*, **158** (1981), pp. 235-244.

[2] D. T Borup, S. A. Johnson, and M. J. Berggren, Nonperturbative diffraction tomography via Gauss-Newton iteration applied to the scattering integral equation, *Ultrasonic Imaging*, **14** (1992), pp. 69-85.

[3] D. T. Borup, S. A. Johnson, and J. W. Wiskin, *FDTD and Integral Equation simulation of a Prototype Ultrasound Breast Scanner*, in Progress in Electromagnetics Research Symposium, (PIERS) July 24-28, University of Washington, Seattle, WA, 1995, p. 621.

[4] Committee on Groundwater Cleanup Alternatives, National Research Council, *Alternatives for Ground Water Cleanup,* National Academy Press, Washington, DC, 1994.

[5] Spyglass, 2-D and 3-D display software, Fortner Research LLC, 100 Carpenter Drive, Sterling, VA 20164.

[6] G.C. Ng, P.D. Freiburge, W.F. Walker, and G.E. Trahey, *A technique for adaptive imaging in the presence of distributed aberrations*, in Proceedings of the 1995 IEEE Ultrasonics Symposium, Seattle, WA, Nov. 7-10, 1995, to appear.

[7] S. A. Johnson, D. T. Borup, M. J. Berggren, J. W. Wiskin, and R. Eidens, *Modeling of Inverse Scattering and Other Tomographic Algorithms in Conjunction with Wide Bandwidth Acoustic Transducer Arrays for Towed or Autonomous Sub-bottom Imaging Systems*, in Proceedings of the IEEE Oceans '92 Conference, Oct 26-29, IEEE Press, New York, NY, 1992, Vol. 1, pp. 294-299.

[8] S.A. Johnson, M.J. Berggren, D.T. Borup, J.W. Wiskin, R.S. Eidens, and H. Leng, *Comparison of Inverse Scattering and Other Tomographic Imaging Algorithms Using Simulated and Tank Data for Modeling Subbottom Imaging Systems*, in Proceedings of the IEEE Oceans '93 Conference, October 18-21, IEEE Press, New York, NY, 1993, Vol. I, pp. 458-492.

[9] Dong-Lai Liu and Robert 'C. Waag, Correction of ultrasonic wavefront distortion using backpropagation and a reference waveform method for time-shift compensation, *J. Acoust. Soc. Am.*, **96** (1994), pp. 649-660.

[10] R. Mallart and Mathias Fink, Adaptive focusing in scattering media through sound-speed inhomogeneities: The van Cittert Zernike approach and focusing criterion, *J. Acoust. Soc. Am.*, **96** (1994), pp. 3721-3732.

[11] L. Nock, G.E. Trahey, and S.W. Smith, Phase aberration correction in medical ultrasound using speckle brightness as a quality factor, *J. Acoust. Soc. Am.*, **85** (1989), pp. 1819-1889.

[12] M. O'Donnel and S. W. Flax, Phase aberration correction using signals from point reflectors and diffuse scatters: Measurements, *IEEE Trans. Ultras. Ferroelec. Freq. Contr.* **35** (1988), pp. 768-774.

[13] M. O'Donnell, E.T. Jaynes, and J.G Miller, Kramers-Kronig relationship between ultrasonic attenuation and phase velocity, *J. Acoust. Soc. Am.*, **69** (1981), pp. 696-701.

[14] T. J. Pearson and A.C.S. Readhead, Image formation by self-calibration, *Annual Review of Astronomy and Astrophysics*, **22** (1984), pp. 97-130.

[15] G. M. Resch, D.E. Hogg, and P.J. Napier, Radiometric correction of atmospheric path length fluctuations in interferometric experiments, *Radio Science*, **19** (1984), pp. 411-422.

[16] S.W. Smith, G.E.Trahey, S.M. Hubbard, and R.F. Wagner, Properties of acoustic speckle in the presence of phase aberration part II: Correlation lengths, *Ultrasonic Imaging*, **10** (1988), pp. 29-51 .

[17] A. Tarantola, *Inverse Problem Theory*, Elsevier, New York, 1987.

[18] J.W. Wiskin, S.A. Johnson, D.T. Borup, M. Berggren, R. Eidens, and Y. Zhang, *Full Inverse Scattering vs. Born-Like Approximation for Imaging in a Stratified Ocean*, in Proceedings of the IEEE Oceans '93 Conference, October 18-21, IEEE Press, New York, NY, 1993, Vol. III, pp. 450-455.

[19] J. W. Wiskin, D. T. Borup, and S. A Johnson, *Inverse Scattering from Cylinders of Arbitrary Cross-Section in Stratified Environments via Green's Operators*, in Progress in Electromagnetics Research Symposium (PIERS), July 24-28, University of Washington, Seattle, WA, 1995, p. 195.

[20] J. W. Wiskin, D. T. Borup, and S. A Johnson, Inverse Scattering from arbitrary 2-D objects in stratified environments via a Green's operator, *J. Acoustic Soc. of Am.* (1995), submitted.

[21] M.S. Zhdanov, *Electromagnetic migration and holography imaging*, in Progress in Electromagnetics Research Symposium (PIERS), July 24-28, University of Washington, Seattle, WA, 1995, p. 679-680.

[22] M.S. Zhdanov, P. Traynin, and O. Portniaguine, Resistivity imaging by time domain electromagnetic migration (TDEMM), *Exploration Geophysics,* **25** (1995), pp. 186-194.